Two-colour In$_{0.5}$Ga$_{0.5}$As quantum dot infrared photodetectors on silicon

Daqian Guo[1] , Qi Jiang[1], Mingchu Tang[1], Siming Chen[1], Yuriy I Mazur[2],
Y Maidaniuk[2], Mourad Benamara[2], Mykhaylo P Semtsiv[3],
William T Masselink[3], Gregory J Salamo[2], Huiyun Liu[1] and Jiang Wu[1]

[1] Department of Electronic and Electrical Engineering, University College London, London WC1E 7JE,
United Kingdom
[2] Institute for Nanoscience and Engineering, University of Arkansas, Fayetteville, AR 72701, United States
of America
[3] Physics Department, Humboldt University Berlin, Newtonstr. 15, D-12489 Berlin, Germany

E-mail: jiang.wu@ucl.ac.uk

Abstract

An InGaAs quantum dot (QD) photodetector is directly grown on a silicon substrate. GaAs-on-Si
virtual substrates with a defect density in the order of 10^6 cm^{-2} are fabricated by using strained-
layer superlattice as dislocation filters. As a result of the high quality virtual substrate, fabrication
of QD layer with good structural properties has been achieved, as evidenced by transmission
electron microscopy and x-ray diffraction measurements. The InGaAs QD infrared photodetector
is then fabricated on the GaAs-on-Si wafer substrate. Dual-band photoresponse is observed at
80 K with two response peaks around 6 and 15 μm.

(Some figures may appear in colour only in the online journal)

1. Introduction

Infrared photodetectors have a number of applications, from civilian to military uses, including night version, medical inspection, optical communications and missile tracking [1, 2]. HgCdTe (MCT) infrared photodetectors, owning to its tuneable bandgap and high quantum efficiency, have dominated the market for years [3]. However, the low production yield and high cost become the bottleneck for further upgrading the HgCdTe-based infrared imaging systems [4]. Over the past two decades, the demand for the third-generation infrared imaging systems brings interests in quantum structures [5–9]. Particularly, III–V quantum structures have been considered as a candidate that could compete with MCT in terms of performance and cost. For instance, quantum dots (QDs) confine charge carriers in all three dimensions, which

promises to reduce dark current, increase operating temperature, and improve detectivity [10, 11]. Moreover, the recent demonstration of the direct growth of III–V QDs on Si substrates has attracted a lot of attentions [12–14]. The monolithic integration of III–V photodetectors with silicon readout integrated circuits (ROICs) opens new opportunities for enhanced functionality and reduction in manufacturing cost [15, 16]. Despite the great promises of monolithic integration of III–V photodetectors and Si ROICs, the epitaxy growth of III–V materials on Si substrates faces great challenges. Due to the large lattice mismatch and difference in thermal expansion coefficient, a high density of threading dislocations (TDs) tends to form at the interface between the Si substrate and III–V epitaxial layers. The TDs propagate into the device active region lead to severe performance degradation. It has been demonstrated that the TD density can be reduced to the extent that the impact on device performance is marginal [12]. Particularly, compared other quantum structures, e.g. quantum wells, QDs are less sensitive to dislocations due to the localization of charge carriers [17]. Although the quantum efficiency of QD infrared photodetectors are yet to be
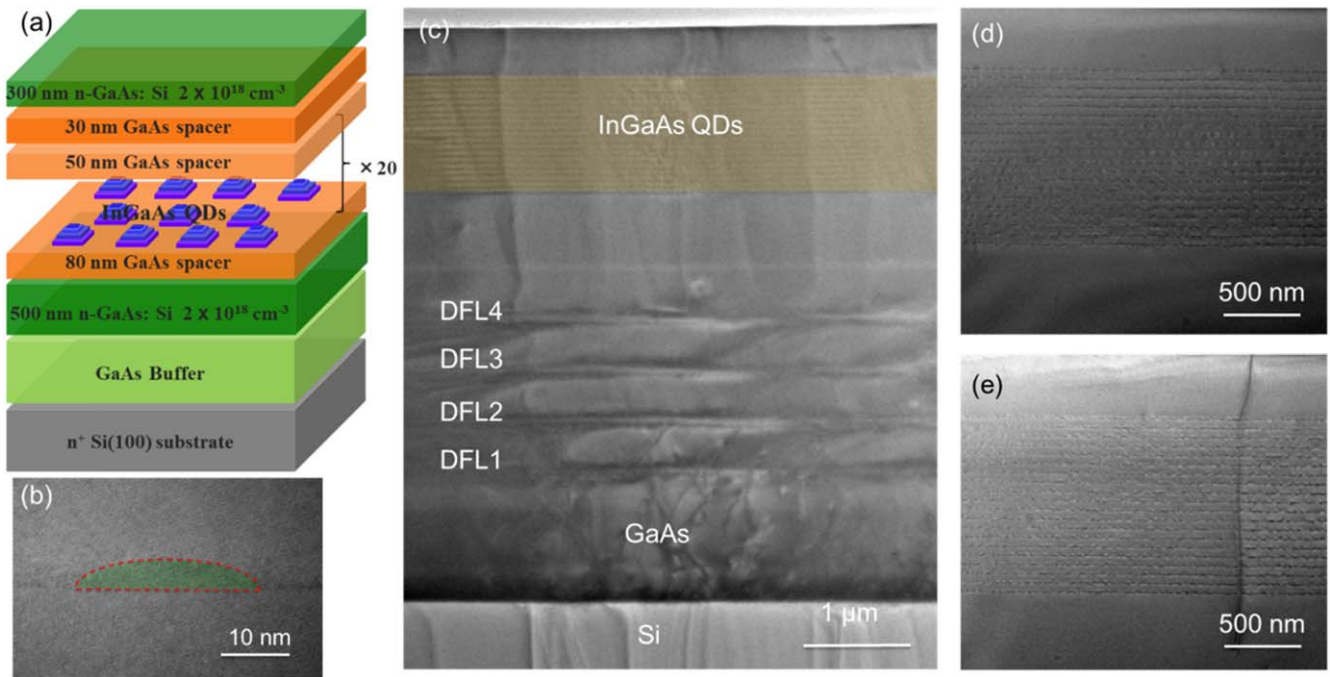
Figure 1. (a) Structure of the QDIP on Si. (b) High resolution TEM image of a single $In_{0.5}Ga_{0.5}As$/GaAs QD grown on Si. (c) Bright filed TEM image showing the entire QDIP and III–V buffer layers on Si. (d), (e) Representative bright filed TEM images of 20 layers of $In_{0.5}Ga_{0.5}As$/GaAs QDs on Si.

improved, the high tolerance of QDs may lead to monolithic integrated large format and low cost QDIPs on Si substrates.

Recently, we have demonstrated InAs/GaAs QD photodetectors directly grown on silicon substrates with a single band photoresponse ($\sim$5–8 μm) [13]. For many applications, multicolour detection is desired. In this paper, a dual-band InGaAs/GaAs QDIP was grown directly on Si by molecular beam epitaxy (MBE). By using InGaAs QDs instead of InAs QDs, multiple intersubband transitions in shallowly confined QDs are possible. The photoresponse covers both atmosphere transmission windows with detection peaks in the mid-wave infrared ($\sim$6 μm) and long-wavelength infrared spectra ($\sim$15 μm).

2. Experimental details

An InGaAs/GaAs QDIP has been directly grown on Si by a solid-source Veeco Gen-930 MBE. Epitaxial growth was taken place on an n-doped Si (100) substrate with 4° offcut towards the [01–1] plane. The device structure is illustrated in figure 1(a). The Si wafer was pre-treated in ultrahigh vacuum over 900 °C for 30 min to remove the surface oxides. Immediately after de-oxidation, the wafer was cooled down for growth. The initiation of growth started with the deposition of a 5 nm AlAs nucleation layer on the Si substrate by migration-enhanced epitaxy at 370 °C. Subsequently, a 1000 nm thick GaAs buffer was deposited followed with four sets of $In_{0.15}Ga_{0.85}As$/GaAs strained-layer superlattices (SLSs) for defect reduction. $In_{0.50}Ga_{0.50}As$/GaAs QDIP epilayers were grown in a sequence as follows: 500 nm n-type GaAs (Si dopant, 2×10^{18} cm^{-3}) bottom contact layer, 80 nm undoped GaAs spacer layer, 20 periods of $In_{0.50}Ga_{0.50}As$/GaAs QDs separated by 50 nm GaAs spacers, and 300 nm n-type GaAs top contact layer (Si dopant, 2×10^{18} cm^{-3}). The QD region was directly doped with about two electrons per dot. The x-ray diffraction measurements are performed by using a Jordan Valley Bede D1 system. The surface morphology of the sample is measured by a Veeco Dimension-3100 atomic force microscopy (AFM) in tapping-mode. Structural analysis was performed by cross-sectional transmission electron microscopy (TEM) at 300 keV using an FEI Titan 80–300 TEM fitted with a CEOS image corrector.

Detectors in circular mesa structure were fabricated by standard photolithography and wet chemical etching techniques. Ni/GeAu/Ni/Au metals were deposited on both bottom and top n^{+}-GaAs contact layers by a thermal evaporator. The metals were annealed to form ohmic contacts by a rapid thermal processing system. Spectral response of the detectors was recorded by a Bruker Equinox-55 Fourier transform infrared spectrometer at 80 K. The device was configured normally to a glow-bar broadband infrared light source. Photocurrent signal was amplified using a SR570 low-noise current preamplifier that also applies a bias voltage to the device and then converted to spectral response by Fourier transform.

3. Results and discussion

Figures 1(b)–(e) shows the cross-sectional TEM images of the QDIP grown on Si. A typical QD has a diameter of about 27 nm and height of 5 nm. The cross-sectional TEM
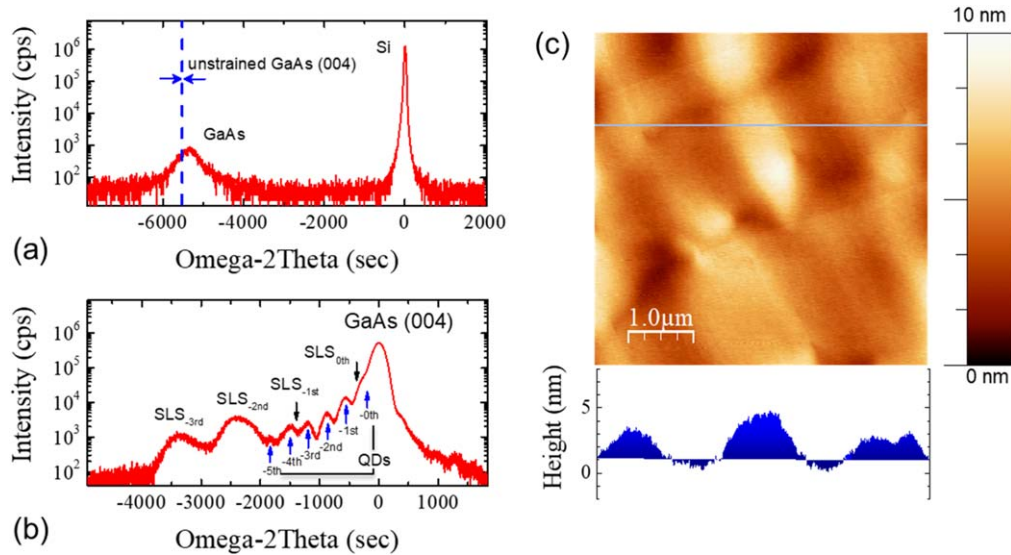
Figure 2. (a) XRD ω-2θ scans for the symmetric Si (004) reflection and (b) ω-scans for the GaAs (004) reflection. (c) A representative AFM image (5 μm × 5 μm) and an AFM line profile of the QDIP.

micrographs show a high density of TDs formed at the GaAs/ Si interface, as shown figure 1(c). Some of the TDs were self-annihilated within the 1000 nm GaAs buffer, but about 10^9 cm^{-2} TDs propagate into the following epilayers and reach the InGaAs/GaAs SLSs. In the low misfit In$_{0.15}$Ga$_{0.85}$As/GaAs layers, gliding of existing mobile TDs assists strain relaxation via introducing misfit dislocations, of which the strain fields enhance the motion of other TDs [18]. As a result, these InGaAs/GaAs SLSs can act as TD filters and reduce the density of TDs by a few orders. The density of TDs is reduced to the level of 10^6 cm^{-2}, estimated by cross-sectional TEM measurements, after the fourth set of SLSs. As shown in figures 1(c)–(e), only a low defect density is visible in the device region with the assistance of InGaAs/ GaAs SLSs.

Symmetric (004) x-ray ω-2θ scans were performed. The results are plotted in figures 2(a) and (b), showing the ω-2θ curves for the Si (004) and GaAs (004) reflections, respectively. Figure 2(a) shows a full width at half maximum (FWHM) as high as 548 arcsec of the GaAs (004) peak in the ω-2θ curve obtained from the Si (004) plane. The FWHM is directly related to the dislocation density, and the high value of the FWHM indicates a high density of dislocations. However, it should be noted that measured GaAs peak is located at around −5350 arcsec, while an unstrained GaAs layer has a (004) symmetric peak separation of −5538 arcsec with respect to the Si (004) peak [19]. This position difference indicates that the GaAs layer is not fully relaxed and under compressed strain. As the device is grown on a thick buffer (>3 μm), the GaAs layers in the active region are expected to be fully relaxed. Therefore, the probed GaAs may be the highly defective GaAs materials at the GaAs/Si interface region. The ω-2θ curves measured nearly the unstrained GaAs (004) reflection is shown in figure 2(b). The FWHM of the GaAs (004) peak is about ∼226 arcsec, which indicate a high quality of the fully relaxed GaAs layers. The dislocation density ρ_d is estimated to be ∼4 × 10^7 cm^{-2}, based on the

relation $\rho_d = (\text{FWHM}/2b)^2$, where b is the Burgers vector [20]. The estimated dislocation density is much higher than the TEM measurements because the highly defective GaAs buffer layers also contribute to the FWHM of the GaAs (004) peak due to the deep penetration depth of x-rays. In addition, clear satellite peaks of QD layers are observed up to the fifth order, which confirms the high quality of the epilayers in the device region. The rather broad peaks separated by about 1000 arcsec are the satellite peaks of InGaAs/GaAs strained superlattice layers. To further visualize the quality of the grown material, AFM image is shown in figure 2(c). The AFM line profiles shows surface undulation up to 5 nm, which is due to strain relaxation of lattice-mismatched hetero-epitaxy [21]. Additionally, the anisotropic strain relaxation of GaAs causes the distinct surface undulation in the orthogonal $\langle 011 \rangle$ directions [21]. Nonetheless, a relatively smooth surface free of antiphase domain has been achieved with a root mean square roughness of 1.4 nm measured from an area of 5 μm × 5 μm.

The temperature-dependent dark current–voltage characteristics for an InGaAs QDIP is shown in figure 3(a). The dark current increases rapidly with increase in the bias voltage due to field-assisted tunnelling of charge curriers. Despite similar dislocation density as the previous study, the InGaAs QDIP shows a higher dark current density (3.95 × 10^{-3} A cm^{-2} at 60 K and 7.55 × 10^{-3} A cm^{-2} at 80 K, both at 1 V) [13]. To gain further insight into the electronic transport mechanism of the device, the dark currents measured under +0.1 V bias from 50 to 300 K are plotted in figure 3(b). In sharp contrast to our previous study [13], the dark current increases rapidly even at low temperatures <100 K, at which thermionic emission is suppressed. As shown in figure 3(b), two activation energies, $E_{a1} = 31$ meV and $E_{a2} = 57$ meV, can be extracted from the dark currents measured at the low-temperature region. The two activation energies correspond to the longitudinal optical phonon energy E_{LO} and $2E_{LO}$, respectively. A dominated
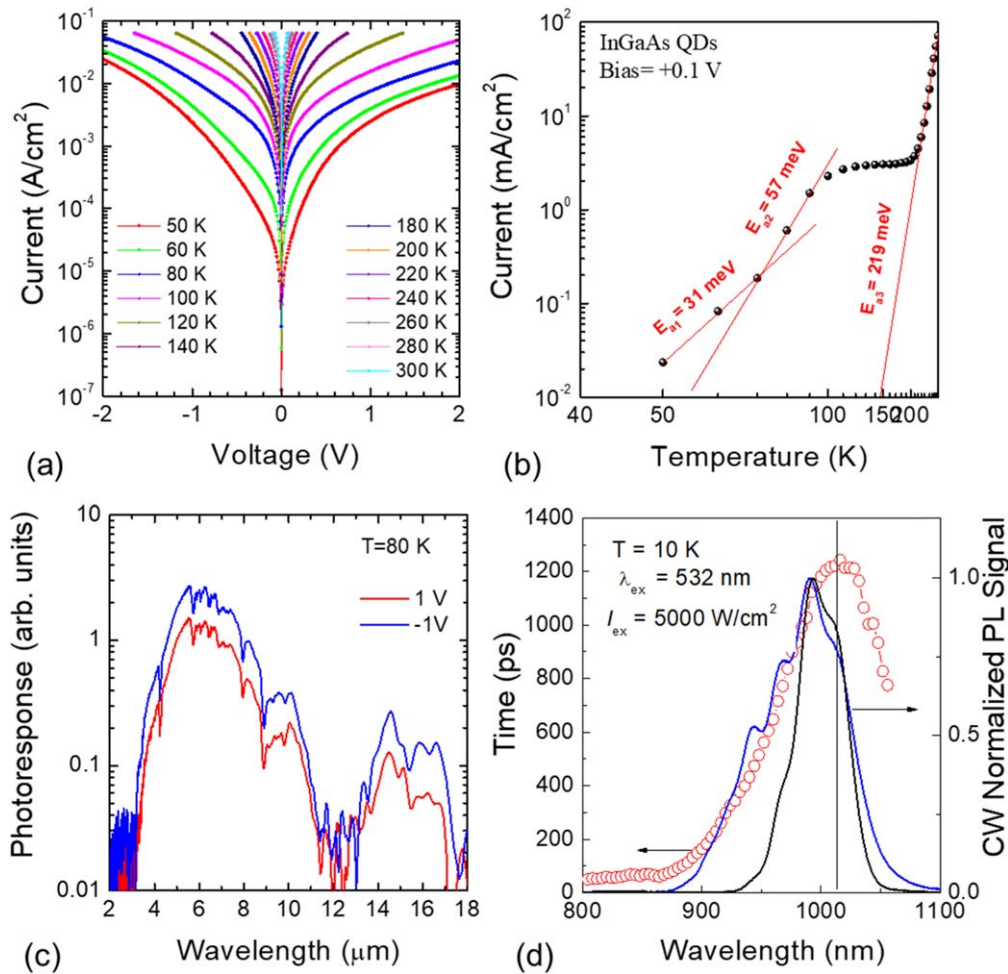
Figure 3. (a) *IV* characteristics measured at different temperatures from 50 to 300 K. (b) Dark current measured under +0.1 V bias at various temperatures. (c) Photoresponse spectra measured with ±1 V at 80 K. (d) Steady state photoluminescence spectra of the In$_{0.5}$Ga$_{0.5}$As QDIP measured with low and high power excitation (5000 W cm^{-2}) at 10 K. The red open circles are the measured photoluminescence decay time at different transition energies.

phonon-assisted tunnelling may be the reason for the high dark current at low temperatures. With further increasing temperature, the increase in dark current is mainly caused by the thermionic emission of charge carriers. By fitting with Arrhenius equation, the thermal activation energy is calculated as $E_{a3} = 219$ meV. This energy corresponds to the transition energy from the highest state occupied by electrons to the conduction band continuum. The QDs are only doped with $2e$/dot, and the electrons are just enough to fully occupy the ground state of the QDs. Therefore, the dark current activation energy E_{a3} matches the energy difference between the ground state of the QDs and the GaAs barrier conduction band edge. Figure 3(c) shows photoresponse spectra measured from the InGaAs QDIP at 80 K. The photoresponse spectra show a dual broadband response from 4 up to 17 μm, covering both the atmosphere transmission windows in the infrared region. Similar to the dark current measurement, photoresponse spectra acquired at both negative (+1 V) and negative (−1 V) voltages show minor difference due to slight structural asymmetry of QDs. The mid-wave infrared band has a peak around ~6.1 μm (203 meV). The transition energy matches well with the thermal activation energy measured

from the dark current measurements, indicates optical transitions from the bound states in the QDs to continuum states. The long-wavelength band with $\Delta\lambda/\lambda_p \sim 10\%$ may be attributed to bound-to-bound transitions. To gain further insight into the electronic structure of the QDs, steady state photoluminescence (PL) and transient PL were carried out at 10 K. As shown in figure 3(d), there are two dominated peaks around 1.25 and 1.22 eV for both low (black curve) and high excitations (blue curve). As both peaks appear at relatively low excitation, they may come from the ground states of QDs with two different sizes. The bimodal distribution of QDs is also evidenced in the transient PL. As shown in figure 3(d), optical transitions at the energies of both peaks show similar long decay time over 1 ns, indicating optical transitions from ground states. At high excitation, two additional PL peaks are observed at 1.29 and 1.31 eV. As the peaks at 1.29 and 1.31 eV have distinctly different decay times, they are assigned as transitions from the first excited state and the second excited state. Assuming the hole levels are closely packed, the energy separation between the ground states and the second excited state to range from 60 to 90 meV, which correspond to 13.7–20.6 μm. It should be noted that the PL
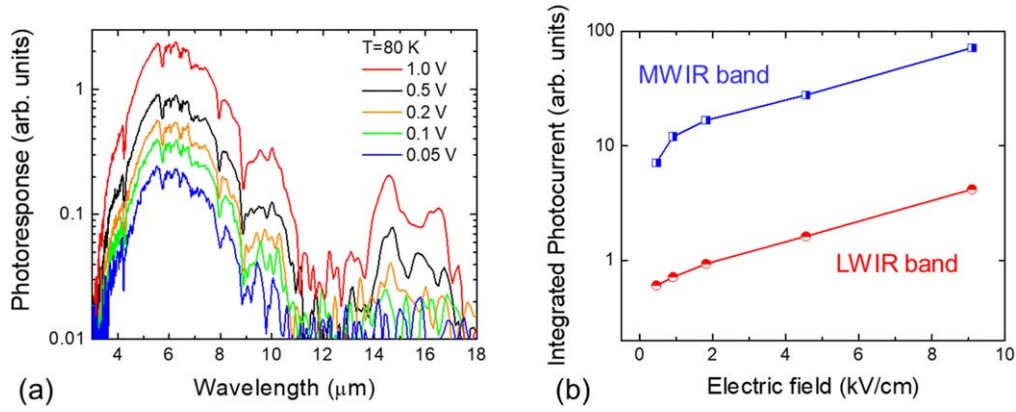
Figure 4. (a) Photoresponse spectra measured with different bias voltages at 80 K. (b) Integrated photocurrent as a function of electric field for both MWIR and LWIR bands.

measurements were carried out at 10 K. At 77 K, it would be expected that the ground state of the smaller QDs was depopulated and the intersublevel transition was mainly from the large QDs with a lower ground state. Considering the slight reduced energy bandgap at 77 K, the transition energy of 90 meV matches with the transition energy of the long-wavelength photoresponse band, 72.9–88.6 meV. Additionally, assuming 70% of the bandgap difference is in the conduction band, the energy separation from the electron ground state to conduction band continuum calculated from the PL data is about 189–210 meV, which matches very well with the mid-wavelength photoresponse peaked at 6 μm and the dark current activation energy. This confirms that the transition of the mid-wavelength band between the ground state to continuum states.

The voltage-dependent photoresponse measurement is carried out, as shown in figure 4(a). The detectors were configured normal to the unpolarized IR source. The intensity of both bands increases monotonically with bias voltage. The behaviour can be understood by the capture rate of photo-excited carriers. With increasing electric field, the electron velocity increases and at the same time, the external field lowers the build-in potential barriers and decreases the capture probability. The intensity of the long-wavelength infrared band is much lower than that of the mid-infrared one. The lower intensity can be explained by a higher potential barrier and hence lower escape rate for photo-excited carriers. This is in agreement with our assumption of bound-to-bound transitions for the long-wavelength infrared band. The voltage-dependent photocurrents of both bands are compared in figure 4(b). The integrated photocurrents of both band show similar dependence with bias voltage at high electric field. However, at low electric field, the photocurrent of the mid-wave infrared band increases much faster. The photocurrent from QDIPs can be written as [22]

$$I_{\text{photo}} = \frac{\delta q n N_{\text{QD}} \Phi}{p_k},\tag{1}$$

where δ is electron capture cross-section coefficient, q is electron charge, n is the average number of electrons per QD, N_{QD} is the areal QD density, Φ is the photon flux density, and

p_k is the capture probability. The capture probability is related to potential barrier height as follows [22, 23]

$$p_k \propto \frac{\tau_{\text{trans}}}{\tau_{\text{life}}} \propto \tau_{\text{trans}} \exp^{-\frac{V_b}{k_{\text{B}}T}},\tag{2}$$

where τ_{trans} and τ_{life} are the transit time and the capture time, V_b is the potential barrier height, and k_{B} is the Boltzmann constant. From equations (1) and (2), it can be the photocurrent of the long-wavelength infrared band is due to a higher potential barrier, in agreement of the assumption of bound-to-bound transitions. When the bias voltage is large enough to overcome the potential barrier, the photocurrents of both bands increase exponentially with the same trend, as shown in figure 4(b). To increase the long-wavelength band response, it may require design of low energy transitions from bound-to-quasi-band in the QDs.

4. Conclusion

A dual-band photoresponse InGaAs/GaAs QDIP is directly grown on the Si substrate by MBE. The low misfit strained InGaAs/GaAs layers significantly reduce the dislocation density by about three orders to the level of $\sim 10^6$ cm^{-2}. TEM and XRD measurements confirms the high crystal quality of the III–V epitaxial grown on Si. The dark current is measured to be 7.55×10^{-3} A cm^{-2} at 80 K and 1 V, much higher than previous work, suggesting further optimization of QDs is required. Given the relatively low TD density, the presence defective QDs may attribute to the dominated phonon-assisted tunnelling dark current. Photocurrent measurements show two photoresponse bands covering both mid-wave infrared and long-wavelength infrared regions, from 4 to 17 μm. The InGaAs QDIP may be promising for monolithically integrated multi-spectral imagers on silicon.

ORCID iDs

Daqian Guo ⓘ https://orcid.org/0000-0002-7350-0925
Huiyun Liu ⓘ https://orcid.org/0000-0002-7654-8553

References

[1] Razeghi M and Nguyen B-M 2014 Advances in mid-infrared detection and imaging: a key issues review *Rep. Prog. Phys.* **77** 082401

[2] Wu J, Li Z, Shao D, Manasreh M O, Kunets V P, Wang Z M, Salamo G J and Weaver B D 2009 Multicolor photodetector based on GaAs quantum rings grown by droplet epitaxy *Appl. Phys. Lett.* **94** 171102

[3] Itsuno A M, Phillips J D and Velicu S 2012 Mid-wave infrared HgCdTe nBn photodetector *Appl. Phys. Lett.* **100** 161102

[4] Simingalam S, VanMil B L, Chen Y, DeCuir E A, Meissner G P, Wijewarnasuriya P, Dhar N K and Rao M V 2014 Development and fabrication of extended short wavelength infrared HgCdTe sensors grown on CdTe/Si substrates by molecular beam epitaxy *Solid-State Electron.* **101** 90–4

[5] Tian Z-B and Krishna S 2015 Mid-infrared metamorphic interband cascade photodetectors on GaAs substrates *Appl. Phys. Lett.* **107**

[6] Unil Perera A G, Lao Y-F, Wolde S, Zhang Y H, Wang T M, Kim J O, Schuler-Sandy T, Tian Z-B and Krishna S S 2015 InAs/GaAs quantum dot and dots-in-well infrared photodetectors based on p-type valence-band intersublevel transitions *Infrared Phys. Technol.* **70** 15–9

[7] Wu J, Shao D, Dorogan V G, Li A Z, Li S, DeCuir E A, Manasreh M O, Wang Z M, Mazur Y I and Salamo G J 2010 Intersublevel infrared photodetector with strain-free GaAs quantum dot pairs grown by high-temperature droplet epitaxy *Nano Lett.* **10** 1512–6

[8] Hoang A M, Dehzangi A, Adhikary S and Razeghi M 2016 High performance bias-selectable three-color short-wave/mid-wave/long-wave infrared photodetectors based on type-II InAs/GaSb/AlSb superlattices *Sci. Rep.* **6** 24144

[9] Wolde S, Lao Y-F, Unil Perera A G, Zhang Y H, Wang T M, Kim J O, Schuler-Sandy T, Tian Z-B and Krishna S 2017 Noise, gain, and capture probability of p-type InAs-GaAs quantum-dot and quantum dot-in-well infrared photodetectors *J. Appl. Phys.* **121**

[10] Wu J, Chen S, Seeds A and Liu H 2015 Quantum dot optoelectronic devices: lasers, photodetectors and solar cells *J. Phys. D: Appl. Phys.* **48**

[11] Lee S J, Ku Z, Barve A, Montoya J, Jang W Y, Brueck S R, Sundaram M, Reisinger A, Krishna S and Noh S K 2011 A monolithically integrated plasmonic infrared quantum dot camera *Nat. Commun.* **2** 286

[12] Chen S *et al* 2016 Electrically pumped continuous-wave III–V quantum dot lasers on silicon *Nat. Photon.* **10** 307–11

[13] Wu J *et al* 2016 Monolithically integrated InAs/GaAs quantum dot mid-infrared photodetectors on silicon substrates *ACS Photonics* **3** 749–53

[14] Wan Y *et al* 2017 Monolithically integrated InAs/InGaAs quantum dot photodetectors on silicon substrates *Opt. Express* **25** 27715–23

[15] Burguete C G *et al* 2018 Direct growth of InAs/GaSb type II superlattice photodiodes on silicon substrates *IET Optoelectron.* **12** 2–4

[16] Kim H, Ahn S Y, Kim S, Ryu G, Kyhm J H, Lee K W, Park J H and Choi W J 2017 InAs/GaAs quantum dot infrared photodetector on a Si substrate by means of metal wafer bonding and epitaxial lift-off *Opt. Express* **25** 17562–70

[17] Liu A Y, Srinivasan S, Norman J, Gossard A C and Bowers J E 2015 Quantum dot lasers for silicon photonics *Photonics Res.* **3**

[18] Ward T, Sánchez A M, Tang M, Wu J, Liu H, Dunstan D J and Beanland R 2014 Design rules for dislocation filters *J. Appl. Phys.* **116**

[19] Orzali T, Vert A, O'Brien B, Herman J L, Vivekanand S, Hill R J W, Karim Z and Rao S S P 2015 GaAs on Si epitaxy by aspect ratio trapping: analysis and reduction of defects propagating along the trench direction *J. Appl. Phys.* **118**

[20] Tapfer L, Martinez J R and Ploog K 1989 Structural investigation by x-ray diffraction of GaAs epilayers and AlAs/GaAs superlattices grown on ⟨100⟩ Si by MBE *Semicond. Sci. Technol.* **4** 617–21

[21] Lam P, Wu J, Tang M, Jiang Q, Hatch S, Beanland R, Wilson J, Allison R and Liu H 2014 Submonolayer InGaAs/GaAs quantum dot solar cells *Sol. Energy Mater. Sol. Cells* **126** 83–7

[22] Martyniuk P and Rogalski A 2009 Insight into performance of quantum dot infrared photodetectors *Bull. Pol. Acad. Sci. Tech. Sci.* **57**

[23] Mitin V, Sergeev A, Vagidov N and Birner S 2013 Improvement of QDIP performance due to quantum dots with built-in charge *Infrared Phys. Technol.* **59** 84–8